Chemical Physics 150 (1991) 281–293
North-Holland

Second-order Raman effects, inelastic neutron scattering and lattice dynamics in 2H–WS_2 ☆

C. Sourisseau [1], F. Cruege and M. Fouassier
Laboratoire de Spectroscopie Moléculaire et Cristalline, U.R.A. 124–C.N.R.S., Université de Bordeaux I, F 33405 Talence, France

M. Alba
Institut Laue–Langevin, B.P. 156 X, F 38042 Grenoble, France

Received 26 June 1990; in final form 27 September 1990

The resonance Raman spectra of 2H–WS_2 single crystals are investigated in detail in the region of low-energy indirect transitions including two direct transitions characterized by A and B exciton peaks. The spectra reveal the activities of first-order resonance Raman signals as well as of second-order Raman (SOR) processes due to coupling phonons with a non-zero momentum. In addition, the longitudinal acoustic (LA) dispersion curves in the (00ζ), (ζ00) and (ζζ0) directions were determined using coherent inelastic neutron scattering (INS) techniques: It is concluded that the more intense SOR band at 352 cm^{-1} is due to the 2×LA(K) overtone, while other SOR peaks can be assigned to combinations of sum or difference bands involving phonons at the K point coupled to the LA(K) mode. Consequently, we have made use of all these data to fix some unknown parameters in complete valence force field lattice dynamics calculations which reproduce satisfactorily the essential features of the Raman and INS results. Also, values of some elastic constants (C_{11}, C_{33}, C_{44}) are estimated and compared with literature data. In agreement with recent band-structure calculations, it is thus definitively concluded that the direct gap nature of the A and B excitons in 2H–WS_2 is responsible for the enhanced intensity of first-order Γ-point phonons (A_{1g}), whereas the K-point phonons, which contribute to the indirect gap absorption edge, are enhanced in the two-phonon resonance Raman spectra: Distinct and simultaneous first- and second-order resonance Raman scattering mechanisms are thus taking place in this material.

1. Introduction

The layered (2D) transition metal dichalcogenides MX_2 are rather attractive systems because they present many unusual physical and chemical properties which are not commonly encountered in three-dimensional materials. In particular, molybdenum and tungsten disulphides and diselenides form a class of semiconducting 2D compounds with a trigonal prismatic coordination of the metal ions in their most common 2H-polytype (fig. 1); their hexagonal unit cell ($P6_3/mmc$) consists of two chalcogenide–metal–chalcogenide sandwich layers linked by relatively weak van der Waals interactions [2].

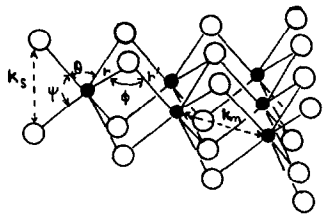

Fig. 1. The structure of bonding within a layer in 2H–WS_2 and definitions of the intralayer internal coordinates.

The structural and electronic properties of these compounds have been reviewed extensively by Wilson and Yoffe [3]. For instance, it is well established that 2H–MoS_2 and 2H–WS_2 are indirect gap semiconductors but present also direct low energy transitions (in the 1.9–2.5 eV range) polarized in the layer planes and characterized by an A–B excitonic pair

☆ A preliminary short version of this work was presented at a recent conference [1].

[1] Author to whom correspondence should be addressed.

[4]. However, up to now the location in the Brillouin zone (at Γ, A, M or K points ...) and the nature of the transitions, to which A and B excitons belong, have been debatable and it must be recalled that band-structure calculations have already been performed on MoS_2, $MoSe_2$ and WSe_2 compounds but have not yet been published for the related WS_2 compound. Nevertheless, following Wilson and Yoffe [3], many authors have attributed in these materials the A–B exciton pair to transitions split by spin–orbit coupling, as suggested by the dependence of the splittings on the masses of the constituent elements; however, in some calculated band structures the smallest direct gap was situated at Γ [5–7] whereas other calculations yielded a direct gap at K [8–12]. To summarize, at least two quite distinct electronic schemes can still be proposed (fig. 2): In a first model (fig. 2a) the A and B peaks are due to d→d type transitions at the centre of the Brillouin zone (Γ) from the filled d_{z^2} metal orbitals to a pair of $d_{x^2-y^2}$, d_{xy} states split by spin–orbit coupling; in a second model (fig. 2b), quite recently developed by Coehoorn et al. [11,12] using the augmented spherical wave method and photoelectron spectroscopic results, the A and B excitons should now correspond to the smallest direct gaps at K (the zone edge point in the (ζζ0) direction) and to transitions from $d_{x^2-y^2}$, d_{xy} states to d_{z^2} type states split by interlayer interactions and spin–orbit coupling. It must be pointed out that in both models the A and B excitons correspond to (x, y) polarized transitions as expected [3,4] and that

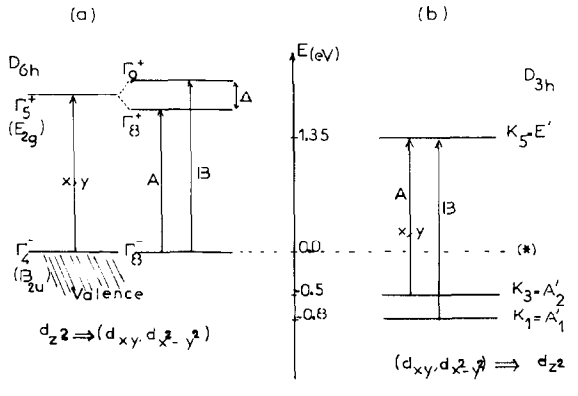

Fig. 2. Electronic schemes for the A and B excitonic transitions proposed in the literature at Γ (a) and K (b) and symmetry assignments of the various levels (see text).

the top of the valence band is localized on the Γ_4^- (B_{2u}) level whereas the bottom of the conduction band is along the line T of the hexagonal Brillouin zone, halfway between the Γ and K points; in addition, only the more recent calculations [11,12] have shown that the Γ_4^- state is not a nonbonding metal d state but rather is an antibonding state, between metal d_{z^2} and non-metal p_z orbitals, a result which explains the high stability of these compounds against photocorrosion in electrochemical cells [13].

Under these conditions one may expect different resonance Raman processes when using laser excitations encompassing these electronic transitions since direct type transitions (near Γ or K) seem to be superimposed to an indirect gap absorption and various electron–phonon coupling mechanisms could take place [14,15]. Indeed, previous Raman studies of 2H–MoS_2 and WS_2 [16–20] have demonstrated the activity of second-order Raman (SOR) processes involving phonons with non-zero momentum; using the inelastic neutron scattering (INS) data along the (ζ00) direction reported by Wakabayashi et al. [21], these SOR effects were recently interpreted for 2H–MoS_2 as due to multiphonon bands involving the longitudinal acoustic LA mode at the M point but for 2H–WS_2 speculative similar assignments were only proposed since INS data were lacking.

We have thus focussed our attention mainly on the 2H–WS_2 compound and investigated in detail the resonance Raman spectra of single crystals using various exciting laser lines covering the whole absorption-edge region and encompassing the A and B transitions; some Raman spectra were also recorded using various incident laser powers and at different temperatures. In addition, we have determined by coherent INS techniques the longitudinal acoustic LA interlayer mode dispersion curves mainly in the (ζ00) and (ζζ0) directions, concentrating on the Brillouin zone edge points at M and K, respectively; in effect, it seems crucial to establish the assignment of the LA coupling phonon (at M or K) which is enhanced on the SOR spectra. Consequently, we have readily assigned most multiphonon SOR peaks and made use of all these data to perform complete lattice dynamics calculations which reproduce the whole dispersion curves.

This paper is thus organized as follows: in section

3.1, we shall present and discuss the various resonance Raman spectra of 2H–WS_2 single crystals including the intensity Raman excitation profiles obtained for the three more intense bands. In section 3.2, the LA dispersion curves determined by INS measurements will be discussed in order to propose confident assignments of the SOR peaks and to get a better insight into the electron–phonon coupling mechanisms; values of some elastic constants will be estimated and compared with literature data. Finally, in section 3.3, the results of complete lattice dynamics calculations will be presented in order to check if one can consistently reproduce the essential features of all experiments.

2. Experimental part

Single crystals of 2H–WS_2 were prepared by means of chemical transport methods according published procedures [2,13]. Raman scattering measurements were performed using ten different exciting lines (in the 676.4–457.9 nm range) of Spectra–Physics Kr^+ and Ar^+ cw lasers and using the T800 (Coderg) or Z 24 (Dilor) triple monochromator instruments with standard photon counting techniques; the slits were adjusted for a spectral band pass of roughly ~ 3–4 cm^{-1}. The experiments were carried out on the near-backscattering geometry and by spinning the laser light on cleaved or as grown (001) surfaces of the sample at 300 K. The relative Raman intensities were estimated by use of the 465 cm^{-1} band of $KClO_4$ as an external standard. Raman spectra ($\lambda_0 = 514.5$ nm) at various temperatures (173–343 K) were also recorded on the OMARS 89 instrument (Dilor) equipped with a microscope objective (100×) in conjunction with a Chaixmeca microthermometry apparatus.

The INS dispersion curves were determined on the triple axis IN8 instrument at the I.L.L. (Grenoble, France) using a ~ 2 mm thick rectangular large single crystal with a surface area of about 30×10 mm^2. The mosaic spread of the sample about the a^*- and c^*-axes was checked on various reflection lines and found to be approximately ~ 1–$2°$ (fwhm) which is acceptable for standard phonon measurements. The crystal was mounted so that the c^*-axis was always in the scattering plane. Both monochromator and analyser were either pyrolitic graphite (PG 002) or copper crystals (Cu 111) and the corresponding energy of neutrons incident on the sample was either 14.7 or 34.8 meV. During the allocated beam time we have mainly determined the phonon LA dispersion branches along the $\Sigma(\zeta 00)$ and $T(\zeta\zeta 0)$ lines for various reduced $|q|$ values, namely equal to 0.04, 0.05, 0.10, 0.20, 0.25, 0.30, 0.33, 0.40 and 0.50 in the former case and to 0.05, 0.10, 0.20, 0.25, 0.30 and 0.33 in the latter one. Along these directions, some additional TA phonons were investigated only for low $|q|$ values since a progressive loss of intensity of the phonon groups accross the zone prevented completion of these TA branches with a good accuracy. Finally, TA and LA phonon energies were also determined at the zone boundary A point (001). Most of the measurements were carried out in the constant wavevector mode of operation but some LA modes at near the zone centre were determined in the constant energy mode. The shape of the sample combined with the small scattering cross sections render the measurements difficult and time-consuming to obtain good statistics. Therefore, we have often used variable neutron energy ranges and counting times and we have repeated experiments around the strongest Bragg spots, namely (002), (100), (006), (110), (008) and (200), in agreement with the theoretically calculated neutron scattering structures factors; the uncertainties in the wavenumbers are thus in general ~ 5–10%.

3. Results and discussion

3.1. Resonance Raman results

The 2H-polytype WS_2 crystallizes in the non-symmorphic D_{6h}^4 space group ($Z=2$); it has 18 modes of lattice vibrations at the centre of the hexagonal Brillouin zone:

$$\Gamma_{vib} = A_{1g} + (2B_{2g}) + E_{1g} + 2E_{2g} + 2A_{2u} + (B_{1u}) + 2E_{1u} + (E_{2u}) .$$

Only four modes A_{1g}, E_{1g}, E_{2g}^1 and E_{2g}^2 are Raman active and have Raman tensors as follows:

$$A_{1g}\begin{pmatrix} a & & \\ & a & \\ & & b \end{pmatrix};$$

$$E_{1g}\begin{pmatrix} & & \\ & & c \\ & c & \end{pmatrix}, \begin{pmatrix} & & -c \\ & & \\ -c & & \end{pmatrix};$$

$$E_{2g}\begin{pmatrix} & d & \\ d & & \\ & & \end{pmatrix}, \begin{pmatrix} d & & \\ & -d & \\ & & \end{pmatrix}.$$

In back-scattering experiments on a surface perpendicular to the c-axis the E_{1g} phonon is forbidden whereas A_{1g} and E_{2g} ones are allowed. Also, the E^2_{2g} phonon (the "rigid-layer" mode) is expected in the very low frequency region [16,17]. Some typical polarized Raman spectra (100–450 cm^{-1}) of 2H-WS_2 at 300 K using a variety of exciting radiations are shown in fig. 3. In agreement with previous studies [17–20] these spectra display two bands due to zone centre active modes at 421 cm^{-1} (A_{1g}) and 356 cm^{-1} (E^1_{2g}) and numerous asymmetric multiphonon bands (noted "s" in fig. 3) whose intensities are drastically laser energy dependent. In particular, it is remarkable that the strongest SOR band at 352 cm^{-1} is more intense than the E^1_{2g} mode when in exact resonance with the A exciton (λ_0=647.1 nm) and than both the E^1_{2g} and A_{1g} modes when using a laser energy in the vicinity of the B excitonic transition (λ_0=530.9 nm). Then, most of these SOR signals nearly disappear using higher laser energies in the vicinity of the C-type electronic band (λ_0=465.8 nm). Therefore, we have obtained the Raman excitation profiles of the three modes at 421, 356 and 352 cm^{-1} when comparing their relative Raman intensities with that of the 465 cm^{-1} band of the ClO_4^- anion (fig. 4). These profiles are corrected for the instrumental response but not for the absorption and reflection coefficients of the sample: For the A_{1g} and E^1_{2g} modes they are in good agreement with those previously published by Sekine et al. [18]; the Raman profile of the SOR peak is reported for the first time. It is thus

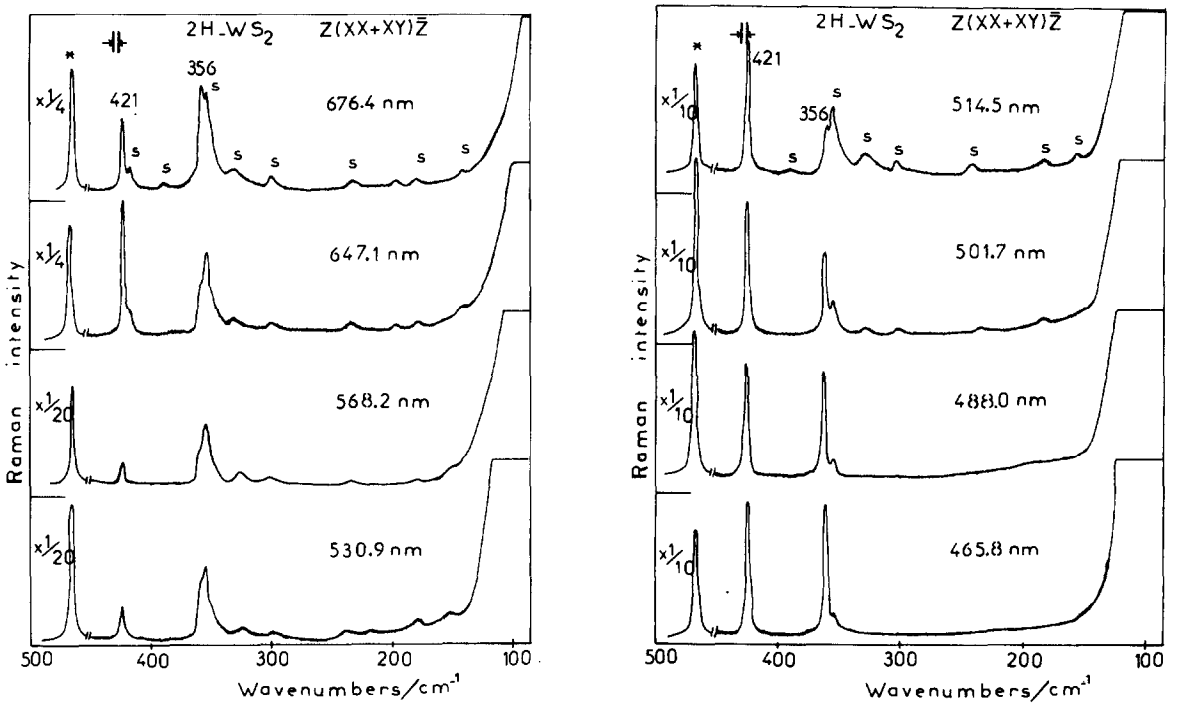

Fig. 3. Polarized Raman spectra (100–450 cm^{-1}) of 2H-WS_2 at 300 K using various exciting lines. * denotes the 465 cm^{-1} band of $KClO_4$ used as external standard, "s" indicates second-order Raman signal, →‖← shows the instrumental resolution.

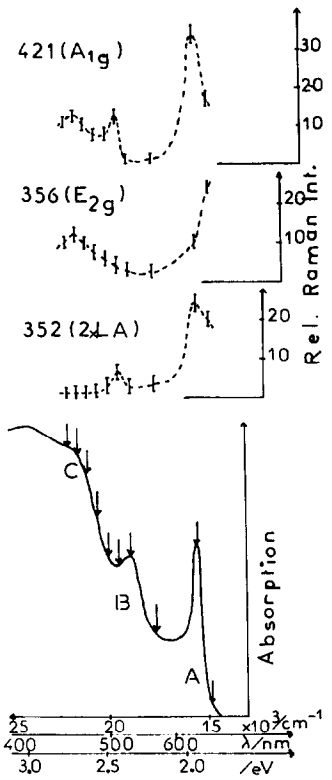

Fig. 4. Comparison of the absorption-edge transmission spectrum of 2H–WS_2 with the Raman excitation profiles of the bands at 421 cm^{-1} (A_{1g}), 356 cm^{-1} (E^1_{2g}) and 352 cm^{-1} (2×LA); arrows indicate the energies of the laser exciting radiations.

clearly evidenced that the intensity profile of the first-order A_{1g} phonon at 421 cm^{-1} gives rise to well-defined maxima near the A (2.0 eV) and B (2.40 eV) transition energies whereas the profile for the E^1_{2g} type mode decreases markedly; then, these first-order signals are enhanced using higher laser energies corresponding to the direct band-to-band C transition at ~2.7 eV (fig. 4). In contrast, the intensity profile of the SOR signal at 352 cm^{-1} decreases significantly as the laser energy increases even though it exhibits weaker maxima near the A and B transitions. We thus conclude that this two-phonon nature signal, whatever its assignment and its momentum or position in the Brillouin zone, must be projected into the totally symmetric representation at Γ and it corresponds to an overtone or combination band of phonons with non-zero momenta ($\pm q$) which contribute to the indirect gap absorption edge; indeed, the two-phonon Raman scattering spectra are more enhanced at the lower laser energies. So, in agreement with Cardona et al. [14], the above results show that this effect may occur for certain phonons, namely those whose $|q|$ equals that of the resonant excitations and may lead to SOR signals due to two phonons of equal and opposite momentum; some examples of such a scattering have already been reported [14,15].

In order to ascertain the nature of the resonance Raman processes and of the SOR signals, we have also recorded some Raman spectra on the one hand with increasing laser power and on the other hand over a wide temperature range. In the former case we have used the 647.1 nm laser line with a power ranging from 10 to 60 mW on the front surface of the sample imbedded in $KClO_4$ and contained in a sample holder rotating at ~2000 rpm in order to avoid any local heating. Linear intensity variations as a function of the laser power were always observed for the first-order bands at 465 cm^{-1} (ClO_4^-) and 421 cm^{-1} (A_{1g}) as well as for the SOR band at 352 cm^{-1}. This allows us to definitively rule out the existence of complex multiphoton processes leading to transitions originating from vibrationally or electronically excited states [22]. In the latter case, we have used the 514.5 nm laser line (~15 mW) and a micro-Raman instrument equipped with a multichannel detector in order to compare simultaneously the intensity variations of the bands at 421 cm^{-1} (A_{1g}) and 352 cm^{-1} (SOR) as a function of the temperature over the 343–173 K range (fig. 5). On theoretical grounds, a one-phonon process may be distinguished from a two-phonon process as the temperature dependence for the first is $(1+n)$ and for the second $(1+n)^2$; the intensity of the second band is thus expected to decrease more significantly as the temperature decreases. Obviously such a process is not effective since, neglecting the very weak linewidth and frequency variations, the SOR band at 352 cm^{-1} is weaker than the first-order signal at 343 and 273 K, has nearly the same intensity at 223 K and becomes the more intense band at 173 K (fig. 5); it is also noteworthy that the first-order component at 356 cm^{-1} (a shoulder) is no longer detected at low temperature.

In agreement with the above discussed Raman spectra (fig. 3), these results can in part be explained by the existence of a red-shift in the energy of the whole indirect gap absorption at low temperature [3].

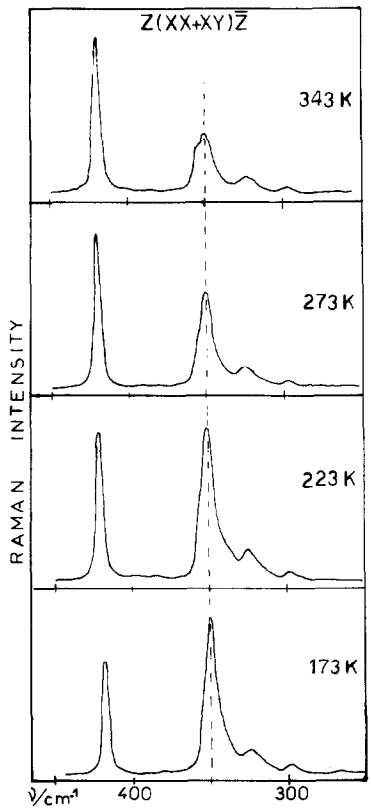

Fig. 5. Polarized Raman spectra (250–450 cm^{-1}) of 2H-WS_2 at various temperatures (343–173 K) using the 514.5 nm laser line.

Therefore, as previously underlined by Stacy and Hodul [20], we hesitate to interpret the temperature dependences of these spectra as due to a large temperature dependence of the magnitude and energy of the resonant absorption bands [23]. Such large changes in the optical properties with temperature complicate the analyses and it seems much better to argue on the basis of the band-shapes in SOR signals. Indeed the complete Raman spectrum (50–800 cm^{-1}) recorded at 173 K (fig. 6) shows that all the multiphonon bands are asymmetric with tails to the lower and higher frequency side for the combination bands that are sum and difference bands, respectively. This allows us to propose the tentative assignments reported in table 1, although at this stage of the discussion the assignment of the LA(K) coupling mode is not established (see below). Nevertheless, whatever the Brillouin zone edge position considered, K or M, the dispersion curve of the LA mode versus momentum is expected to have an inverse parabolic shape and the electronic transitions of wave vector $K \pm \delta$ or $M \pm \delta$ (for small δ) will couple to phonons of corresponding momentum. Under these conditions, the more intense SOR signal is assigned as twice the fundamental frequency of a LA mode and other new bands are combinations of sum (in the higher frequency region) and of difference (in the low frequency part) bands coupled to this LA mode. One can thus predict that the frequencies of the $A_{1g}(K_1)$, $B_{2g}(K_2)$, $E^1_{2g}(K_5)$ and $E_{1g}(K_6)$ modes at the K point here considered are roughly equal to 409, 371, 348 and 310 cm^{-1}, respectively. Another band of medium intensity at 524 cm^{-1} and weaker signals at 297 and 268 cm^{-1} remain to be assigned and they could correspond either to other 2LA-type modes along T or more likely to higher-order difference bands between the projection of the 2LA mode at Γ and an E^2_{2g} progression. Indeed, on going from 324 to 268 cm^{-1} a regular spacing of 27–30 cm^{-1} is observed and the intensities decrease drastically; moreover, from symmetry arguments such vibrational couplings can be favoured.

We thus conclude that the SOR spectra of 2H-WS_2 under resonance conditions are better understood, provided the assignment of the LA(K) coupling mode is confirmed by INS experiments.

3.2. *Inelastic neutron-scattering study*

As coherent inelastic neutron scattering data for 2H-WS_2 are lacking and SOR effects in 2H-MoS_2 were already explained involving the LA mode at the M point (16, 20), we have looked at the LA dispersions curves in the (00ζ), ($\zeta 00$) and ($\zeta\zeta 0$) directions concentrating on zone edges at A, M and K, respectively. All the experimental points obtained for various $|q|$ values are reported in fig. 7.

First of all, it is convenient to classify the various branches in terms of their group theoretical representations. In the (00ζ) direction there are four irreducible representations Δ_1, Δ_2, Δ_5 and Δ_6; Δ_1 and Δ_2 are non-degenerate and each of them contains three branches which are purely longitudinal (LA); Δ_5 and Δ_6 are doubly degenerate and contain six branches which are purely transverse ($TA_\parallel$). There are also four irreducible representations in the ($\zeta 00$) directions,

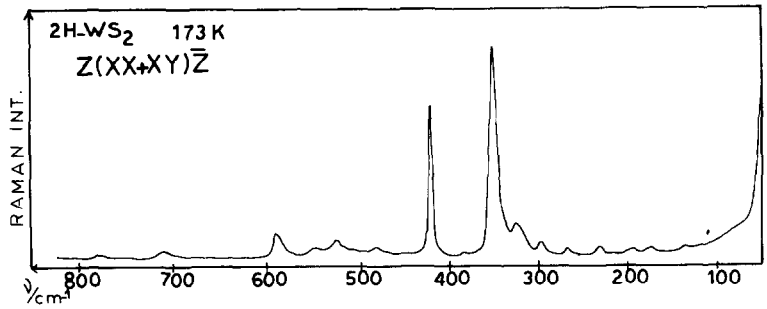

Fig. 6. Complete Raman spectrum (50–850 cm^{-1}) of 2H-WS_2 at 173 K using the 514.5 nm laser lines and an optical multichannel instrument.

Table 1
Raman bandwavenumbers (cm^{-1}) and assignments for 2H-WS_2 at 173 K (λ_0=514.5 nm)

ν/cm^{-1}	int.	Assignments		
		1st order at Γ	2nd order at K	higher-order (?)
27.4 [a]		E^2_{2g}		
138	vw		E_{1g}–LA	
173	w		E^1_{2g}–LA	
198	vw		B_{2g}–LA	
233	m		A_{1g}–LA	
267	vw		–	2LA–$3E^2_{2g}$
297	m		–	2LA–$2E^2_{2g}$
306 [a]		E_{1g}	–	
325	ms		–	2LA–E^2_{2g}
352	ms		2×LA(K)	
356	sh	E^1_{2g}	–	
380	vw		–	2LA+$2E^2_{2g}$
416 [b]	w		LA+TA?	
421	s	A_{1g}	–	
482	w		E_{1g}+LA	
523	m		E^1_{2g}+LA	
544	mw		B_{2g}+LA	
585	ms		A_{1g}+LA	
703	w		4×LA(K)	
774	vw		A_{1g}+E^1_{2g}	

[a] From Sekine et al. [17].
[b] Only observed with red exciting lines (676.4 and 647.1 nm).

Σ_1, Σ_2, Σ_3 and Σ_4, all of which are non-degenerate, leading to $6\Sigma_1+2\Sigma_2+6\Sigma_3+4\Sigma_4$ type branches; Σ_2 and Σ_4 are purely transverse modes with polarization vectors parallel to the basal plane ($TA_{\parallel}$) whereas Σ_1 and Σ_3 are neither purely longitudinal nor purely transverse; although these latter modes are of mixed character, the acoustic modes may be regarded to be either mostly longitudinal LA(Σ_1) or mostly transverse $TA_{\perp}$(Σ_3). Finally, for the T line in the ($\zeta\zeta$0) direction, there are also four irreducible representations which give rise to $5T_1+4T_2+4T_3+5T_4$ type branches; non of these are purely longitudinal nor purely transverse but the acoustic modes may be regarded to be mostly longitudinal LA(T_1, T_4) or mostly transverse $TA_{\perp}$(T_3).

In such experiments in the (ζ00) direction for instance, it must be recalled that only the Σ_1 and Σ_3 type branches are detected and expected to be nearly degenerate in pairs, except for the very low frequency region ($\nu \leqslant 3$ THz or 100 cm^{-1}), whereas the Σ_2 and Σ_4 modes with polarization vectors perpendicular to the scattering plane cannot be detected [21].

An overall comparison of the INS data (fig. 7) reveals a weak dispersion along the (00ζ) direction and large frequency variations in the basal plane directions. In particular, the frequency of a phonon along T with a wavevector less than 0.25 (in $|4\pi/a|$ unit) is almost identical to that of its counterpart along Σ; such a phonon dispersion isotropy in the layer planes is not at all surprising for 2D systems [21,24,25]. Furthermore, as compared with INS results along Σ for 2H-MoS_2 [21], one notes a drastic frequency lowering of the LA(Σ_1) curve due to a metal mass effect so that the zone edge frequency at the M point is equal to 142 cm^{-1}. This indicates that there are strong perturbations in the metal vibrational amplitudes on going from 2H-MoS_2 to WS_2. At the K point a quite similar result is obtained but more interestingly, the LA mode frequency increases up to 182 cm^{-1}. Indeed, this last value may be a good candi-

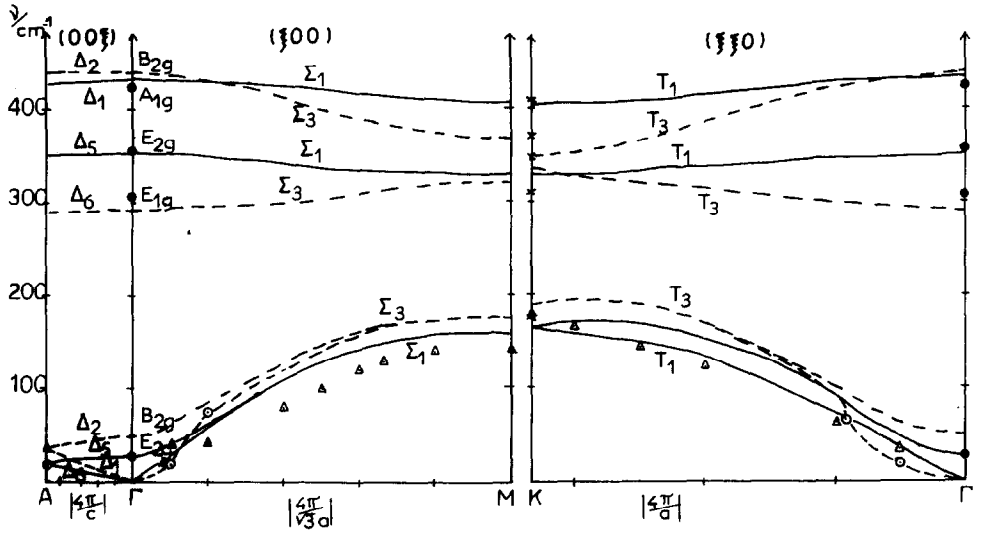

Fig. 7. Dispersion curves of the acoustic and some optic modes in 2H-WS_2 along (00ζ), (ζ00) and (ζζ0) directions as obtained from lattice dynamical calculations (see text) and comparisons with inelastic neutron scattering data (○: TA modes; △: LA modes), with first-order Raman data (●) and with Raman estimates at K from second-order Raman effects (×).

date to account for the very intense SOR signal observed at 352 cm^{-1} [$\sim 2\times$LA(K)] on the resonance Raman spectra. Under these conditions, most multiphonon SOR peaks have been readily assigned to combination of sum or difference bands involving phonons at the K point coupled to the LA(K) mode, as previously discussed (table 1). So, we come to the conclusion that, instead of the LA(M_2) phonon, it is the LA(K_5) type phonon which is more likely to be involved into the electron–phonon coupling mechanisms and the various K-type phonons which contribute to the indirect gap absorption are enhanced in the two-phonon Raman scattering spectra [14]. Surprisingly, such a $|q|$ value for the low energy resonant excitations corresponds to that proposed by Coehoorn et al. [11,12] for the direct $K_3 \rightarrow K_5$(A) and $K_1 \rightarrow K_5$(B) excitonic transitions, even though only the phonons with $|q|=0$ are generally enhanced in the two-phonon spectra as the resonance with direct gaps is approached. Nevertheless, it is noteworthy that, at a first order of perturbation, the LA(K_5) could also be involved in a vibronic coupling ($K_5 \otimes K_5 = K_1+K_3+K_5$) leading perhaps to another source of resonance Raman enhancement; alternatively, the weak maxima observed on the Raman excitation profile of the 2LA(K) mode (fig. 4) could be also explained by some participation of indirect electronic transitions in the A and B excitons.

Finally, even though extensive INS measurements were not performed at very small momentum transfers, one notes very small initial slopes near the zone centre in the INS curves for the $TA_\perp$ modes in the (ζ00) and (ζζ0) directions as it is expected for an hexagonal structure. The initial slopes of these branches are also required by symmetry (rotational invariance) to be equal to that of the TA(Δ_6) mode in the (00ζ) direction. Therefore, the elastic constants C_{11}, C_{33} and C_{44} are thus estimated and found equal to 158 ± 16, 60 ± 5 and $16\pm2\times10^9$ N/m^2, respectively. As shown in table 2, these constants can nicely be compared with related values in other 2D chalcogenide compounds [25,26]. It is noteworthy that the anisotropy of elastic properties is weak since the ratio of the longitudinal sound velocity parallel and perpendicular to the basal plane,

$$v_\parallel / v_\perp = (C_{11}/C_{33})^{1/2},$$

does not exceed 2.5 for the materials listed here. According to Sandercock [27], this weak anisotropy in the sound velocity arises from the partial compensation due to anisotropy in the lattice parameters and is in contrast with the strong anisotropic bonding (see

Table 2
Elastic constants (in 10^9 N/m^2) in some 2D chalcogenides

	$TiSe_2$ [a]	$TiSe_2$ [b]	2H–$NbSe_2$ [c]	2H–$TaSe_2$ [d]	2H–MoS_2 [e]	2H–WS_2 [f]	2H–SnS_2 [g]
C_{11}	–	120	~169	169	174	158±16	146
C_{33}	54.6	39.0	50.9	53	46.6	60±5	27.2
C_{44}	17.9	14.3	21.2	17.4	25.0	16±2	8.3
$(C_{11}/C_{33})^{1/2}$	–	1.75	1.82	1.78	1.93	1.62	2.31

[a] See [31]. [b] See [32]. [c] See [33]. [d] See [28]. [e] See [21]. [f] This work. [g] See [27].

below) since the bulk elastic properties depend both on the length and number density of the interatomic springs.

3.3. Lattice dynamics calculations

Before drawing definitive conclusions, we have made use of all the above results to carry out complete valence force field calculations. As a matter of fact, such a theoretical approach may allow us to fix some unknown parameters and to check if one can consistently reproduce the essential features of the data, in particular the INS results.

Considering that the intralayer bondings in these compounds are mainly covalent in character whereas the interlayer interactions are assumed to be of van der Waals type between the sulfur atoms of neighboring layers, Wakabayashi et al. [21] for 2H–MoS_2 have first made use of a potential function including five valence force type parameters, K_r, $K_{rr'}$, K_θ, K_ϕ and K_ψ (fig. 1) and of two axially symmetric type parameters α_1, α_2 corresponding to central "radial" and "transverse" forces between the sulfur atoms (table 3). In fact the α_1 and α_2 parameters represent the compressional and shearing components of the force constants for each pair of interacting atoms; they are defined as

$$\alpha_1 = \left.\frac{d^2V}{dr^2}\right|_{r=R} \quad \text{and} \quad \alpha_2 = \frac{1}{r}\left.\frac{dV}{dr}\right|_{r=R},$$

where V is the interatomic potential and R is the equilibrium distance between sulfur atoms of neighboring layers. INS results in the $(\zeta 00)$ and (00ζ) directions were thus correctly fitted although the restriction on the force constants imposed by the rotational invariance was not satisfied since the elastic constant C_{44} calculated from Σ_3 and Δ_6 (TA) curves was different almost by a factor of 2.0 [21]. Then, Feldman [28] has proposed a dynamical matrix including only valence force field parameters in which the interlayer S–S interactions were considered to be given directly by the first- and second-neighbor bond-stretching force constants; under these conditions the force constants are defined as follows:

$$\alpha_i = \left.\frac{d^2V}{dr^2}\right|_{r=R_i} \quad (i=1,2),$$

where R_1 and R_2 are the equilibrium distances between the first- and second-neighbor sulfur atoms in the van der Waals gap. From an extensive study of different phenomenological lattice dynamical models for 2H–$TaSe_2$ and 2H–$NbSe_2$ compounds, Feldman concluded that in future comparison with experiment it should be kept in mind that, as in the case of MoS_2, the short-range proposed models could be

Table 3
Values of the force constants ($\times 10^2$ N/m) in 2H–MoS_2 and 2H–WS_2 used in lattice dynamics calculations

Cts [a]	2H–MoS_2			2H–WS_2
	Ref. [21]	Ref. [28]	this work	this work
K_r	1.3846	1.385	1.385	1.385
K_s	–	–	–	0.17
K_m	–	–	−0.12	−0.12
$K_{rr'}$	−0.1722	−0.1722	−0.17	−0.17
K_θ	0.1502	0.1502	0.045	0.143
K_ϕ	0.1892	0.1892	0.294	0.180
K_ψ	0.1381	0.1381	0.138	0.138
α_1	0.0311	0.0198	0.020	0.030
α_2	0.0072	0.0258	0.026	0.020

[a] Intralayer internal coordinates are defined in fig. 1 and for interlayer force constants (α_1, α_2) see discussion in the text.

somewhat inadequate with regard to optic-mode dispersions along Σ [28]. Indeed, later on Schönfeld et al. [29] have shown that the calculated ratios of anisotropic mean-square displacements between the two atom types were not in agreement with experimental findings; in addition, we have checked that the Feldman's model reproduces with a good agreement the experimental results at Γ but with a poor one along Σ and T (table 4). Therefore, we have modified K_θ and K_ϕ values which could not be entirely determined at Γ, where only their sum $(K_\theta + K_\phi)$ is meaningful [30], and included an additional parameter K_m equal to -0.12×10^2 Nm^{-1} corresponding to the near-neighbor Mo–Mo interactions in the layer planes (table 3). Under these conditions a satisfactory agreement between experimental and calculated frequencies is obtained whatever the Γ, A, M or K point considered (table 4); in particular, we have checked that LA dispersion curves are particularly well fitted whereas TA curves are overestimated. It must be pointed out that the calculated LA mode frequencies at M and K can be well compared (228 and 242 cm^{-1}, respectively) so that, in contrast with previous studies [16,20], SOR signals in 2H–MoS_2 could be interpreted also as due to the LA(K) coupling phonon; the two-phonon resonance Raman effects in 2H–MoS_2 could require an entirely new discussion.

Similarly, we have carried out complete valence force field calculations for 2H–WS_2 and included one additional parameter $K_S = 0.17 \times 10^2$ Nm^{-1}, which corresponds to a near-neighbor S–S central force constant, i.e. between intralayer sulfur atoms whose interatomic spacing is along the *c*-axis (fig. 1); this improves the quality of the fits mainly at the K point. Values of α_1 and α_2 parameters were also adjusted to fit LA and TA frequencies at the A point and K_θ and K_ϕ parameters were slightly perturbed, as compared with the previously proposed quantities in 2H–MoS_2 [21,28], in order to improve the quality of the fits along the Σ and T lines (tables 4 and 5). As shown in fig. 7, we thus obtain a satisfactory agreement not only between the INS data and the calculated LA dispersion curves, but also between the Raman estimates at K and the zone edge calculated phonon wavenumbers (table 5). It is noteworthy that these calculations confirm the strong metal-mass dependence of the LA mode frequencies which are now equal to 159 cm^{-1} (M) and to 165 cm^{-1} (K) at the zone boundaries. Simultaneously, the TA mode frequencies appear not at all metal-mass dependent so that, as above mentioned for 2H–MoS_2, the TA branches along Σ and T lines are again overestimated. This leads us to the quite unusual calculated results $\Sigma_3 > \Sigma_1$ and $T_3 > T_1$ at the zone edges [25]; precise adjustements of the corresponding TA branches must await additional INS measurements.

Considering the approximations used, this simple model seems to reproduce the main features of the experimental results but there are still some discrepancies clearly outside of the experimental uncertainties for large values of the wavevector. According to Wakabayashi et al. [21] to improve the model it would be necessary to include the polarizability of sulfur and/or some additional cross terms in the potential function. Nevertheless, from these calculations we confirm again that the observed two-phonon resonance Raman effects in 2H–WS_2 can be explained by SOR processes involving the LA mode at the K point of the Brillouin zone.

4. Conclusion

From Raman, resonance Raman, INS data and lattice dynamics calculations we conclude that SOR scattering by phonons with non-zero momentum involving mainly the LA(K_5) type mode occurs in the layered group VIA 2H–WS_2 compound when in resonance with the low energy indirect gap absorptions even though two direct A and B excitonic-type transitions are also known to exist in this region. This result is in contrast with the generally accepted idea that strong SOR spectra are characteristic for metallic 2H-polytype group VA transition metal dichalcogenides and are not observed for the analogous group VIA semiconducting compounds [27]. Then under the assumption that the A and B excitons in 2H–WS_2 correspond to the smallest gaps at K [11,12], it appears that these electronic transitions could be vibronically coupled to the LA(K_5) type phonon, and we suggest that similar coupling mechanisms are probably effective in the related 2H–MoS_2 compound.

Finally, it must be pointed out that from a resonance Raman study we have obtained information not only about the electronic band-structure but also

Table 4
Results of complete lattice dynamics calculations for 2H–MoS_2 at Γ, M, K and A points and comparison with various experimental data

Γ/D_{6h}	ν_{exp}	ν_{calc}		M/D_{2h}	ν_{exp} INS [21]	ν_{calc}	
		Feldman [28]	this work			Feldman [28]	this work
$A_{1g}(\Gamma_{1+})$	409	413.7	414.1	$A_g(M_{1+})$	397	387.3	400.5
$B_{2g}(\Gamma_{4+})$	(~475)	482.6	483.0	$B_{3g}(M_{3+})$	423	400.9	406
	(~56)	56.9	57.1		174	216.0	172.9
$E_{1g}(\Gamma_{6+})$	287	301.1	301.0	$B_{2g}(M_{2+})$	–	318.8	303.4
				$B_{3g}(M_{3+})$	~360	345.9	338.7
$E_{2g}(\Gamma_{5+})$	383	403.2	403.0	$B_{1g}(M_{4+})$	–	350.7	339.2
				$A_g(M_{1+})$	~350	327.1	339.0
	34	35.1	35.3	$B_{1g}(M_{4+})$	–	233.3	328.9
				$A_g(M_{1+})$	234	236.3	228.4
$A_{2u}(\Gamma_{2-})$	470	477.3	477.8	$B_{1u}(M_{4-})$	425	403.4	408.6
	0	0	0		174 (TA)	216.0	172.9
$B_{1u}(\Gamma_{3-})$	(~410)	403.6	403.9	$B_{2u}(M_{2-})$	~397	391.5	403.1
$E_{1u}(\Gamma_{6-})$	384	400.8	400.6	$B_{2u}(M_{2-})$	~350	349.5	340.9
				$B_{3u}(M_{3-})$	–	356.4	341.4
	0	0	0	$B_{2u}(M_{2-})$	234 (LA)	255.4	228.4
				$B_{3u}(M_{3-})$	–	253.0	228.9
$E_{2u}(\Gamma_{5-})$	(~297)	295.9	295.7	$B_{1u}(M_{4-})$	~360	328.2	340.2
				$A_u(M_{1-})$	–	322.0	306.8

K/D_{3h}	ν_{exp} SOR [16,20]	ν_{calc}		A/D_{6h}	ν_{exp} INS [21]	ν_{calc}	
		Feldman [28]	this work			Feldman [28]	this work
$A_1'(K_1)$	410	383.2	400.8	A_{1g}	–	408.6	408.9
$A_1''(K_2)$	–	377.0	375.3	B_{2g}	–	480.2	480.6
		234.4	187.5		(38)	40.0	40.1
$E''(K_6)$	~296	342.2	366.0	E_{1g}	–	298.5	298.3
$E'(K_5)$	368	345.5	331.9	E_{2g}	–	402.1	401.8
	233	249.7	242.2		(~24)	24.7	24.8
$A_2''(K_4)$		374.4	374.5	A_{2u}	–	480.2	480.6
		234.4	187.5		38 (LA)	40.1	40.1
$A_2'(K_3)$		383.0	400.7	B_{1u}	–	408.6	408.9
$E'(K_5)$	–	345.5	331.9	E_{1u}	–	402.1	401.8
	233 (LA)	249.7	242.2		~24 (TA)	24.7	24.8
$E''(K_6)$		322.8	305.7	E_{2u}	–	298.5	298.3

about the frequency values of several modes in the Brillouin zone. Such relevant data may be of great help in these low-dimensional compounds either to establish suitable lattice dynamical models or to get a better insight into the Raman spectra of some intercalated derivatives since in their ordered phases it is sometimes observed new modes (which become Raman active in first order) due to zone folding mechanisms [26,30].

Table 5
Results of complete lattice dynamics calculations for 2H–WS_2 at Γ, M, K and A points and comparison with various experimental data

Γ/D_{6h}	ν_{exp}	ν_{calc} [a]	M/D_{2h}	ν_{exp} [a] INS	ν_{calc} [a]
$A_{1g}(\Gamma_{1+})$	421	434.4	$A_g(M_{1+})$		406.9
	(436)	438.1			369.0
$B_{2g}(\Gamma_{4+})$			$B_{3g}(M_{3+})$		
	(45)	48.5			173.0
			$B_{2g}(M_{2+})$	–	310.6
$E_{1g}(\Gamma_{6+})$	~306	290.9			
			$B_{3g}(M_{3+})$	–	321.3
			$B_{1g}(M_{4+})$	–	330.8
	356	352.8			
			$A_g(M_{1+})$	–	330.1
$E_{2g}(\Gamma_{5+})$					
			$B_{1g}(M_{4+})$	–	160.6
	27.4	27.8			
			$A_g(M_{1+})$		158.6
	435	430.4		–	371.2
$A_{2u}(\Gamma_{2-})$		0	$B_{1u}(M_{4-})$		
	0	423.4			173.0
$B_{1u}(\Gamma_{3-})$	(420)		$B_{2u}(M_{2-})$	–	407.5
		349.5	$B_{2u}(M_{2-})$		331.4
	356				
$E_{1u}(\Gamma_{6-})$			$B_{3u}(M_{3-})$		332.8
		0	$B_{2u}(M_{2-})$		158.6
	0			~142 (LA)	
		285.7	$B_{3u}(M_{3-})$		160.6
$E_{2u}(\Gamma_{5-})$	(306)		$B_{1u}(M_{4-})$		320.4
			$A_u(M_{1-})$		312.8

K/D_{3h}	ν_{exp} [a] SOR (INS)	ν_{calc} [a]	A/D_{6h}	ν_{exp} [a] INS	ν_{calc} [a]
$A_1'(K_1)$	409	403.6	A_{1g}		426.2
	~371	346.6			437.2
$A_1''(K_2)$			B_{2g}		
	~240	188.5		(~37)	34.2
$E''(K_6)$	310	337.3	E_{1g}		288.1
	348	331.8			351.0
$E'(K_5)$			E_{2g}		
	(176)	165.1		(~19)	19.6
		346.6			437.2
$A_2''(K_4)$			A_{2u}		
		188.5		~37 (LA)	34.2
$A_2'(K_3)$		403.6	B_{1u}		426.2
		331.8			351.0
$E'(K_5)$			E_{1u}		
		165.1		~19 (TA)	19.6
	176 (LA)				
	~(182)				
$E''(K_6)$		314.5	E_{2u}		288.1

[a] This work.

Acknowledgments

Authors are grateful to R. Cavagnat for his technical assistance in Raman measurements and to Dr. Gorochov for a gift of WS_2 single crystals.

Authors have also appreciated the illustrating comments and remarks of the referees.

References

[1] C. Sourisseau, M. Fouassier, M. Alba, A. Ghoroyeb and O. Gorochov, Paper presented at symposium D on Solid State Ionics at the E-MRS Fall meeting, Strasbourg (France), November 1988 and published in: Mater. Sci. Eng. B 33 (1989) 119.
[2] W.J. Schutte, J.L. de Boer and F. Jellinek, J. Solid State Chem. 70 (1987) 207.
[3] J.A. Wilson and A.D. Yoffe, Adv. Phys. 18 (1969) 193.
[4] T.J. Wieting and J.L. Verble, in: Physics and Chemistry of Materials with Layered Structures, Vol. 3, eds. T.J. Wieting and M. Schluter (Reidel, Dordrecht, 1979) p. 381.
[5] R.V. Kasowski, Phys. Rev. Lett. 30 (1973) 1175.
[6] D.W. Bullett, J. Phys. C 11 (1978) 4501.
[7] M. Tanaka, H. Fukutani and G. Kuwabara, J. Phys. Soc. Japan 45 (1978) 1899.
[8] L.F. Matheiss, Phys. Rev. Lett. 30 (1973) 784; Phys. Rev. B 8 (1973) 3719.
[9] K. Wood and J.B. Pendry, Phys. Rev. Lett. 31 (1973) 1400.
[10] S.P. Hind and P.M. Lee, J. Phys. C 13 (1980) 349.
[11] R. Coehoorn, C. Haas, J. Dijkstra, C.J.F. Flipse, R.A. de Groot and A. Wold, Phys. Rev. B 35 (1987) 6195.
[12] R. Coehoorn, C. Haas and R.A. de Groot, Phys. Rev. B 35 (1987) 6203.
[13] V. Douay and O. Gorochov, J. Chim. Phys. 83 (1986) 247.
[14] M. Cardona and O. Guntherodt, in: Light Scattering in Solids II and III, Topics in Applied Physics, Vols. 50 and 51 (Springer, Berlin, 1982) and references therein.
[15] A. Cingolani, M. Lugana and G. Scamarcio, Nuovo Cimento D 10 (1988) 519.
[16] J.M. Chen and C.S. Wang, Solid State Commun. 14 (1974) 857.
[17] T. Sekine, T. Nakashizu, K. Toyoda, K. Uchinokura and E. Matsuura, Solid State Commun. 35 (1980) 371.
[18] T. Sekine, T. Nakashizu, M. Izumi, K. Toyoda, K. Uchinokura and E. Matsuura, J. Phys. Soc. Japan Suppl. A 49 (1980) 551.
[19] T. Sekine, K. Uchinokura, T. Nakashizu, E. Matsuura and K. Yoshizaki, J. Phys. Soc. Japan 53 (1984) 811.
[20] A.M. Stacy and D.T. Hodul, J. Phys. Chem. Solids 46 (1985) 405.
[21] N. Wakabayashi, H.G. Smith and R.M. Nicklow, Phys. Rev. B 12 (1975) 659.
[22] C. Cosse, M. Fouassier, T. Mejean, M. Tranquille, D.P. Dilella and M. Moskowits, J. Chem. Phys. 73 (1980) 6076.
[23] R.F. Frindt and A.D. Yoffe, Proc. Roy. Soc. A 273 (1963) 69.
[24] R.M. Nicklow, N. Wakabayashi and H.G. Smith, Phys. Rev. B 5 (1972) 4951.
[25] H. Bilz and W. Kress, in: Phonon dispersion relations in insulators, Springer Series in Solid-State Sciences, Vol. 10, eds. M. Cardona and P. Fulde (Springer, Berlin, 1979) p. 161.
[26] S. Nakashima, M. Hangyo and A. Mitsuishi, in: Vibrational Spectra and Structure, Vol. 14, ed. J.R. Durig (Elsevier, Amsterdam, 1985) p. 305.
[27] J. Sandercock, Festkörperprobleme 15 (1975) 183.
[28] J.L. Feldman, Phys. Rev. B 25 (1982) 7132.
[29] B. Schönfeld, J.J. Huang and S.C. Moss, Acta Cryst. B 39 (1983) 404.
[30] W.G. McMullan and J.C. Irwin, Can. J. Phys. 62 (1984) 789.
[31] M. Scharli and F. Levy, Phys. Rev. B 33 (1986) 4317.
[32] W.G. Stirling, B. Dorner, J.D.N. Cheeke and J. Revelli, Solid State Commun. 18 (1976) 931.
[33] N. Wakabayashi, H.G. Smith and R. Shanks, Phys. Lett. A 50 (1974) 367.